Front. Energy 2025, 19(6): 1007–1021
https://doi.org/10.1007/s11708-025-1014-4

RESEARCH ARTICLE

Flowerlike CeO_2 used as novel adsorption material for removal of hydrogen fluoride gas from lithium-ion battery during thermal runaway

Haozhe Xu[1#], Shuai Yuan[2#], Chunwen Sun (✉)[1], Donghao Cheng (✉)[2]

1 Beijing School of Chemical and Environmental Engineering, China University of Mining and Technology, Beijing 100083, China
2 China Academy of Civil Aviation Science and Technology, Beijing 100028, China

Abstract Thermal runaway presents a significant challenge for large-scale application of lithium-ion batteries (LIBs), often leading to the release of flammable, explosive, and toxic gases. In this study, porous flowerlike cerium dioxide microspheres (FL-CeO_2) were investigated to eliminate hydrogen fluoride (HF) gas generated during thermal runaway. A dedicated test device and method were developed for this purpose. The FL-CeO_2 was synthesized via a hydrothermal method and coated onto nickel foam to fabricate a gas filter. During thermal runaway of a 5 Ah lithium iron phosphate ($LiFePO_4$) battery, the filter—loaded with 1.2 g CeO_2—achieved an instantaneous HF removal rate of up to 82.24% within approximately 40–50 s. X-ray photoelectron spectroscopy (XPS) results indicate that F^- ions replace O^{2-} ions in the CeO_2 lattice. Additionally, the potential for reusability of the CeO_2 microspheres was evaluated through multiple HF adsorption and desorption cycles. After 10 cycles, the regenerated CeO_2 microspheres retained a HF adsorption rate of 76.11%, demonstrating promising reusability.

Keywords lithium-ion batteries (LIBs), thermal runaway, ceria microspheres, hydrogen fluoride (HF), regeneration

1 Introduction

Lithium-ion batteries (LIBs) have recently gained widespread popularity as energy storage solutions [1]. Although LIBs have great development prospects, safety concerns have become one of the main obstacles restricting their application and development. Many methods have been proposed to enhance the safety of LIBs, such as modeling for health estimation and enhancing the performance of separators to eliminate HF inside the battery [2,3]. However, LIBs are still susceptible to thermal runaway, which can lead to combustion and explosion under mechanical, electrical, or thermal abuse, and the consequences of such incidents are extremely serious [4–7].

During thermal runaway, in addition to the release of intense heat and pressure, a large quantity of dangerous gases is also generated. Current research on gas emission during LIB thermal runaway mainly focuses on their composition, formation mechanisms, and associated hazards. A lithium-ion battery consists of key components such as a cathode, an anode, a separator, and electrolytes [8]. Typically, the electrolyte is composed of a lithium salt, $LiPF_6$, dissolved in a carbonate solvent [9]. When temperatures within the battery exceed 220 °C, violent reactions can occur among the cathode, anode, electrolyte, and binder [4,10]. These reactions produce substantial volumes of flammable gases including CH_4, H_2, C_2H_4, CO_2, and CO, which are the major gases released by LiBs during thermal runaway [11–13]. Yuan et al. [14] tracked temperature escalations in LIBs of various chemistries using an accelerated rate calorimeter. They discovered that CO_2, CO, and H_2 were the primary gases released, accounting for over half of all emissions. Qin et al. [15] induced thermal runaway in a prismatic LFP battery pack and, using hydrogen probes and an FTIR device, discovered that the predominant gases emitted were H_2, CH_4, CO, CO_2, and C_2H_4. When flammable and explosive gases such as CO and H_2 mix

Received Feb. 18, 2025; accepted Apr. 3, 2025; online May 31, 2025
Correspondences: Chunwen Sun, csun@cumtb.edu.cn;
Donghao Cheng, chengdh@mail.castc.org.cn

[#] These authors contribute equally to this work.

with oxygen in a confined space, they can lead to violent explosions, especially under the high temperatures and open flame conditions.

The hazards of thermal runaway are not limited to flammable and explosive gases, as toxic gases such as hydrogen fluoride (HF) also pose significant dangers. Larsson et al. [16] examined thermal runaway in LIBs and reported the production of hazardous HF gas. Zhang et al. [17] found that CO and HF the primary toxic gases released during such events. The toxicity of HF gas is well-documented: it is extremely irritating to human skin and can penetrate deeply, causing necrosis inside the body, which is extremely difficult to treat. In addition, the occupational exposure limit of HF gas is only 2.5 mg/m^3 over a 15-min period [11], suggesting that even low concentrations can cause serious harm. In fact, HF gas is primarily generated through the thermal decomposition of the electrolyte salt lithium hexafluorophosphate ($LiPF_6$) [18]. $LiPF_6$ remains thermally stable at 107 °C in dry conditions with water content under 10 parts per million. However, when water levels reach 300 parts per million, it begins to decompose at approximately 87 °C due to a heat-induced reactions with water vapor, producing phosphorous oxyfluoride (POF_3) and HF. Above 117 °C, HF and POF_3 continue to be released via two further reactions (Reactions 2 and 3), until $LiPF_6$ is completely transformed into lithium fluoride (LiF). The detailed generation process is as follows [19,20].

$$LiPF_6 \rightarrow LiF + PF_5 \quad (1)$$

$$PF_5 + H_2O \rightarrow POF_3 + 2HF \quad (2)$$

$$LiPF_6 + H_2O \rightarrow LiF + POF_3 + 2HF \quad (3)$$

From the above reactions, it can be seen that the presence of water vapor is very important, as it may also accelerate the formation of HF gas [21]. Although the amount of HF gas released during thermal runaway of a single lithium-ion battery is not much, the risk becomes significantly greater in the case of failure propagation. If a large lithium-ion battery pack undergoes thermal runaway, the emission of toxic gases can be extremely harmful, which has attracted great attention [17,22].

However, there are few studies on the rapid adsorption of toxic gases produced during the thermal runaway of LIBs. In recent years, CeO_2 material has emerged as a novel adsorbent for fluoride removal in the field of water purification due to its non-toxic nature and unique redox properties [23–32]. A comparison of various materials is presented in Table S1, in which the fluoride removal performance of CeO_2, commercially available Al_2O_3, and bone char is compared. It can be seen that the fluoride adsorption performance generally shows a positive correlation with specific surface area. Moreover, the morphology and pore structure of the material also affect its adsorption capacity, potentially leading to differences in performance. Due to the existence of the oxygen vacancies, which may facilitate Ce^{3+}-F complexation and ion exchange, CeO_2 also has great potential for fluoride removal [48].

In addition, CeO_2 is known as a unique oxygen storage and release material, and it has demonstrated excellent catalytic activity toward CO. It has been effectively used in the adsorption of CO in automobile exhaust systems [33,34]. Sun et al. [35] developed a hydrothermal method to synthesize nearly uniform, flower-like CeO_2 microspheres with an open, three-dimensional, hollow porous framework, showing great potential for application in catalysis and adsorption.

In this work, a simple test device and method were proposed and designed to evaluate the adsorption performance of gases generated during the thermal runaway of LIBs. Flowerlike CeO_2 microspheres with a three-dimensional porous structure composed of nanosheets were synthesized via a hydrothermal method and successfully applied to the adsorption of toxic HF gas generated during the thermal runaway of LIBs.

2 Experiment

2.1 Synthesis of flowerlike $CeOHCO_3$ microspheres

All chemicals were purchased from Beijing Chemical Reagent Company and used without further purification. Glucose (0.01 mol), acrylamide (0.015 mol), and cerium nitrate hexahydrate (0.005 mol) were added to approximately 80 mL of deionized water and stirred with a magnetic stirrer until the solution became clear. Then, 25 wt% ammonia was added to this clear solution while stirring continuously, adjusting the pH to around 10. After maintaining agitation for 5 h, the solution was transferred to a Teflonlined autoclave and heated in a blast drying oven at 180 °C for 72 h. After the heating process, the autoclave was allowed to cool naturally, and the resulting orange-tinted suspension was centrifuged to separate the solid phase. The resulting solid was rinsed several times with both distilled water and pure ethanol, then dried at 60 °C for 12 h to obtain flowerlike $CeOHCO_3$ microspheres (Fig. S1 in Electronic Supplementary Material).

2.2 Synthesis of flowerlike CeO_2 microspheres

The prepared $CeOHCO_3$ microspheres were calcined in two steps to obtain flowerlike CeO_2 microspheres. First, the prepared product was calcined under an argon atmosphere in a tube furnace at 600 °C for 6 h. Subsequently, the resulting product was further heated in air at 400 °C for 4 h. In both steps, the temperature increased at a rate of 3 °C per min. (Fig. S1).

2.3 Preparation of flowerlike CeO_2 filter

Nickel foam was used as a support because it is resistant to high temperatures and non-flammable, making it well-suited for high-temperature environment generated during thermal runaway of LIBs. Flowerlike CeO_2 was coated onto the nickel foam to fabricate filters. First, a certain amount of flowerlike CeO_2 and 5 wt% (mass fraction) sodium carboxymethyl cellulose (CMC) were added to water and mixed uniformly by sonication for 30 min. Then, the nickel foam was cut into a round filter, and the mixed solution was evenly applied onto the surface. After the solution completely dried, the filter was pressed and held for 2–5 min to form the final structure. Filters coated with different masses of CeO_2 were prepared using the same procedure. As shown in Fig. S2, due to the flexibility of nickel foam and the presence of the binder, the prepared filter is highly flexible and can be folded easily for multiple times, making it suitable for a variety of application scenarios.

2.4 Characterization of materials

X-ray powder diffraction, conducted using a Bruker D8 advance, was employed to analyze the purity and phase composition of the samples. Structural features were observed using scanning electron microscopy (XL30s-FEG at 10 kV) and transmission electron microscopy (JEOL JEM-2100F), which provided insights into the morphology. To determine the surface area and porosity, nitrogen adsorption-desorption isotherm analysis was performed at 77 K using a Micromeritics ASAP 2460. Additionally, the elemental composition and oxidation states within the flowerlike CeO_2 structures were assessed through X-ray photoelectron spectroscopy using a Thermo Scientific K-Alpha device.

2.5 Adsorption experiment

A test device and experimental method were designed to evaluate the HF gas adsorption performance of LIBs during thermal runaway. A sealed box made of 304 stainless steel customized for the experiment. The top of the box was fitted with transparent tempered glass, allowing for observation of the thermal runaway reaction inside. At the rear of the box, a pressure sensor was installed to monitor internal pressure changes, and a set of copper conductors connected the test equipment both inside and outside the box, such as heating plates and thermocouples. As shown in Figs. S3(a) and S3(b), the lithium-ion battery was fixed on the heating plate inside the box, with thermocouples placed on the surface of the battery, the bottom of the heating plate, and the outlet for the thermal runaway gases to measure corresponding temperature changes. The dimensions of the box, as seen in Fig. S3(d), are 550 mm × 400 mm × 400 mm, with all air ports having an outside diameter of 6 mm. Additionally, a simple filter device was designed to securely hold the prepared nickel foam filter inside, as shown in Figs. S3(e) and S3(f).

Recently, the use of gas sensors alongside Fourier transform infrared spectroscopy (FTIR) has become a common practice for monitoring HF emissions from LIBs during thermal runaway [36–38]. While gas sensors tend to be less accurate and more prone to damage, they are far more convenient and suitable for measuring specific gases. Therefore, a gas sensor was selected for this experiment. The HF gas sensor (TB200B) from EC Sense GmbH in Germany was chosen, with a range of 0–500 mg/m^3 and an accuracy of 0.1 mg/m^3. The gas sensor was recalibrated before each experiment, and repeated tests show that the error could be controlled within a specific range.

The experimental setup, shown in Fig. S3(c), includes a simple filter device connected to the gas exhaust line of the lithium-ion battery during thermal runaway, with gas sensors positioned at the gas outlet. To prevent the potential explosion of the lithium-ion battery inside the box after thermal runaway, a vacuum pump was used to extract part of the air in the box (e.g., reducing the pressure to −50 kPa), and nitrogen was introduced to return pressure to normal levels (with a relative humidity of about 56%). All valves, except the exhaust port, were closed. Finally, an electric heating device was utilized to induce thermal runaway in the lithium-ion battery.

3 Results and discussion

3.1 Physical characterization of flowerlike CeO_2 microspheres

X-ray powder diffraction (XRD) was utilized to identify the crystalline phase of the synthesized cerium dioxide, as shown in Fig. S4. The phase of the calcination product was determined to be face-centered cubic cerium dioxide (JCPDS No. 34-0394) with the space group Fm3m (225) [35].

Both scanning and transmission electron microscopy were employed to observe the size and morphology of the specimens. The images, particularly Figs. 1(a) and 1(b), reveal that many of the CeO_2 particles are almost uniform spheres with flowerlike features. These spheres generally range from 1 to 3 μm in diameter. Further analysis, as detailed in Figs. 1(c) and 1(d), shows that these flowerlike spheres consist of numerous nanosheets, which resemble petals. The individual nanosheets are approximately 20–30 nanometers thick, and they interlace to form an open, porous structure.

Figures 1(e) and 1(f) show the TEM images of CeO_2 microspheres. The plane spacing of the ordered fringes in Fig. 1(h) is approximately 0.16 nm, which corresponds to

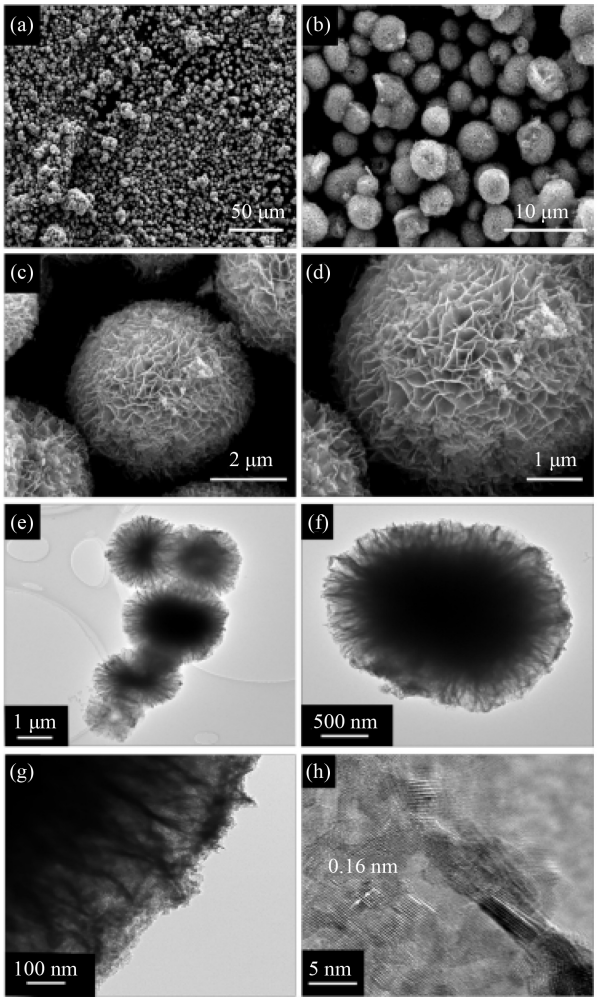

Fig. 1 SEM images of flowerlike CeO_2 microspheres.
(a, b) Overall appearance of flowerlike CeO_2 microspheres; (c, d) an individual flowerlike CeO_2 microsphere; (e) TEM images of overall shape of flowerlike CeO_2; (f, g) TEM images of an individual flowerlike CeO_2 microsphere; (h) HRTEM image of a typical nanosheet.

the (311) lattice plane of CeO_2. Figure 2 shows the nitrogen adsorption–desorption isotherm of the obtained CeO_2 microspheres, along with the corresponding BJH (Barret-Joyner-Halenda) pore size distribution curves. The material exhibits a type IV adsorption–desorption pattern with an H3 hysteresis loop, as seen in Fig. 2(a), indicative of its mesoporous nature. The area of Brunauer-Emmett-Teller (BET) surface area of the CeO_2 microspheres is approximately 129.8 m^2/g. The average pore size, calculated from the nitrogen isotherm adsorption branch in Fig. 2(b) using the BJH method, is 10.25 nm. The corresponding cumulative desorption volume from the BJH analysis is 0.29 cm^3/g.

3.2 Adsorption experiment for the gas generated during thermal runaway of LIBs

All tested batteries were maintained at 100% state of charge, ensuring that the release of hazardous gases during thermal runaway was representative. Lithium-ion phosphate batteries were chosen for the thermal runaway experiments due to their high safety, making them almost impossible to explode. Additionally, they produce gases during thermal runaway, which is the most critical aspect of this experiment. A 5 Ah lithium-ion phosphate battery was chosen for the thermal runaway experiment, because it generates an appropriate concentration of HF gas. The pressure (⩾ 4 kPa gauge) generated in the box by the lithium-ion battery thermal runaway gas ensures that the gases smoothly and quickly exhausted through the only open exhaust port. The filter was placed on the gas path, and the HF gas concentration was measured at the air outlet.

Initially, the experiment was conducted with four pieces of nickel foam filter without CeO_2 coating to rule out the possible effects of the nickel foam itself. As shown in Figs. S8(a) and S8(b), an experiment was also performed without the nickel foam, directly measuring the HF gas concentration from the LIBs thermal runaway.

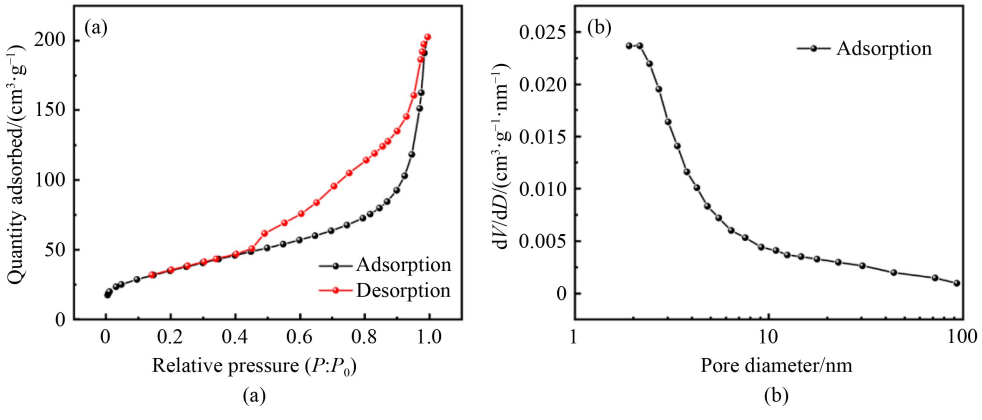

Fig. 2 Flowerlike CeO_2 microspheres.
(a) Nitrogen adsorption–desorption isotherms; (b) corresponding BJH pore size distribution.

The maximum HF gas concentration is 388.5 mg/m^3, suggesting that the presence of nickel foam does not interfere significantly with the experiment.

Next, 0.4 g of CeO_2 was coated onto 2 and 4 pieces of nickel foam, respectively, as filters to study the effect of the number of filters. Adsorption experiments were conducted by coating 0.4, 0.8, 1.2, and 1.6 g of CeO_2 microspheres onto 4 pieces of nickel foam to investigate the effect of mass on adsorption.

Moreover, regeneration and reuse experiments were performed on CeO_2 microspheres which had already undergone adsorption. The filters were sonicated in water for 1–3 h to obtain the CeO_2 coating, then placed in an oven at 60 °C for 2–5 h to remove moisture. The CeO_2-coated filter was then heated in a tube furnace at 800 °C for 60–120 min to remove the internal fluoride ions. Finally, adsorption experiments were carried out following the same method previously described.

Since the thermal runaway gas production of lithium-ion battery is a rapid and dynamic process, four pieces of filter, both without CeO_2 and with 1.2 g CeO_2 microspheres, were placed in the gas path for two groups of experiment. 4 L gas collection bags were used to collect gases generated during thermal runaway in order to estimate the gas production rate. As shown in Videos 2 and 3, the gas collection bags were filled in about 30 s. The estimated gas production rate for both two groups of experiments was approximately 133 mL/s, confirming that the pressure inside the box allows the gases to pass through the filters without any problems.

Figure 3 shows the thermal runaway process of the lithium-ion battery. In Fig. 3(b), it can be seen that as the temperature rose, the battery started to expand due to the gas production at around 95 °C. From Figs. 3(c)–3(e), it can be observed that when the temperature reached approximately 120–130 °C, the battery started to undergo thermal runaway and generated a large volume of gas within 40–50 s. Figure S6 shows the temperature changes of the gases measured by the thermocouple placed at the gas outlet during the thermal runaway of the lithium-ion battery. It can be seen that the gas temperature reaches a maximum of 88.9 °C.

The removal rate ($R\%$) of HF gas at a given moment is calculated by

$$R\% = \frac{C_i - C_n}{C_i} \times 100, \tag{4}$$

where C_i and C_n are the HF gas detection concentration of the filters both without and with CeO_2 coating at a certain time respectively, mg/m^3.

Experiments investigating thermal runaway in LIBs reveal that gas production during such events is dependent on the battery's thermal state. As a battery enters full thermal runaway, gas generation accelerates abruptly. Monitoring typically involves tracking the battery's surface temperature. A sudden spike in temperature, peaking at its maximum value, coincides with the most intense phase of thermal runaway. During this phase, hazardous gases are produced rapidly, with their concentrations peaking when the battery temperature reaches its zenith.

According to the experiments, LIBs experience thermal

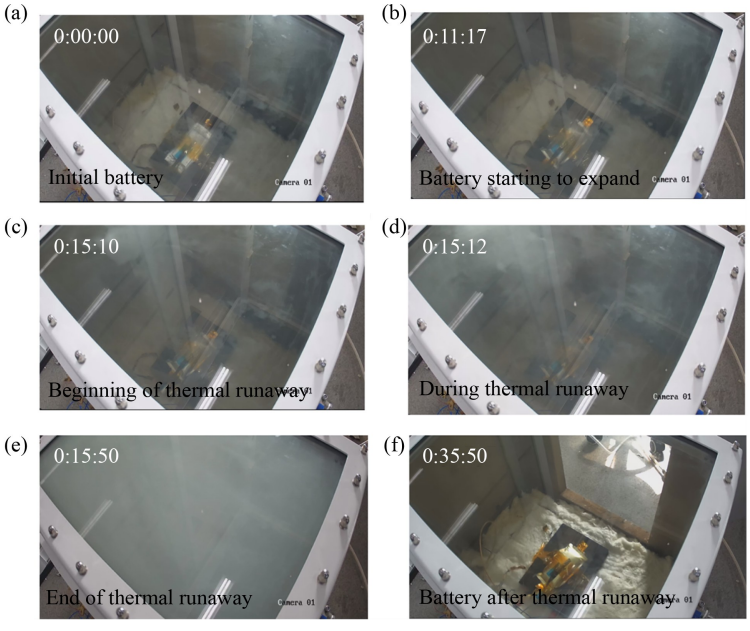

Fig. 3 Thermal runaway experiment of $LiFePO_4$ based lithium-ion battery.

(a) Initial battery; (b) battery starting to expand; (c) beginning of thermal runaway; (d) during thermal runaway; (e) end of thermal runaway; (f) battery after thermal runaway.

runaway between 120 and 130 °C, followed by the production of large amounts of gas. Since the venting valve remains open, the chamber pressure gradually rises and stabilizes between 4 and 7 kPa as the lithium-ion battery temperature reaches its maximum. At this point, the volume of released gas is at its largest, and the concentration of HF gas generated also peaks. Therefore, the ability of the CeO_2 material is evaluated to rapidly remove HF gas based on the detected HF concentration at this time. The highest instantaneous removal rate is calculated accordingly.

Figure 4(a) shows the HF concentration detected with four pieces of nickel foam filter without CeO_2 coating, reaching a maximum concentration of 349 mg/m^3. Figure 4(b) and 4(c) show the HF concentrations detected on two and four pieces of nickel foam filter, each coated with 0.4 g of CeO_2. The highest instantaneous HF concentrations are similar: 112.2 and 117.8 mg/m^3, indicating little difference in filtration efficiency between the two and four filters. Therefore, in later experiments, four pieces of filter were used as the substrate, as they could hold more adsorbent material.

Figures 4(c)–4(f) show HF concentrations when 0.4, 0.8, 1.2, and 1.6 g of CeO_2 were coated on four pieces of nickel foam filter. The highest instantaneous HF concentrations are 117.8, 67, 61.3, and 50.7 mg/m^3, with the corresponding instantaneous removal rates of 66.25%, 80.81%, 82.24%, and 85.47%, respectively.

Due to various factors, such as differences in the production of LIBs and the inherent randomness of the thermal runaway process, the concentration of thermal runaway gas produced by LIBs can vary. Therefore, the experiment was repeated by coating 0.4, 0.8, 1.2, and 1.6 g of CeO_2 on four pieces of nickel foam filters. As shown in Figs. 4(g) and 4(i), and Table 1, the corresponding highest HF concentrations were 109.4, 73.8, 48.6, and 41.5 mg/m^3, with instantaneous HF removal rates of 68.66%, 78.86%, 86.08%, and 88.11%,

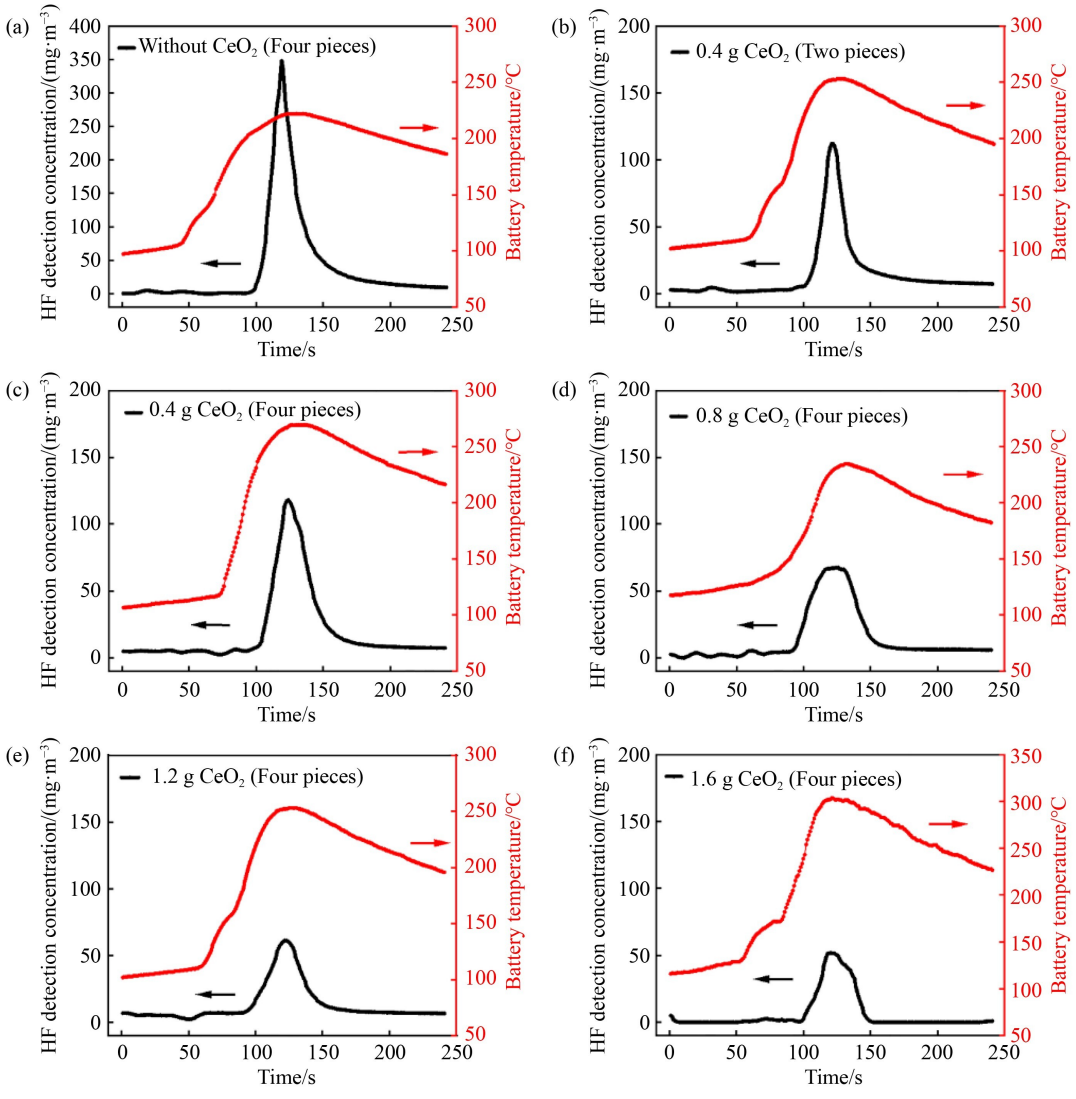

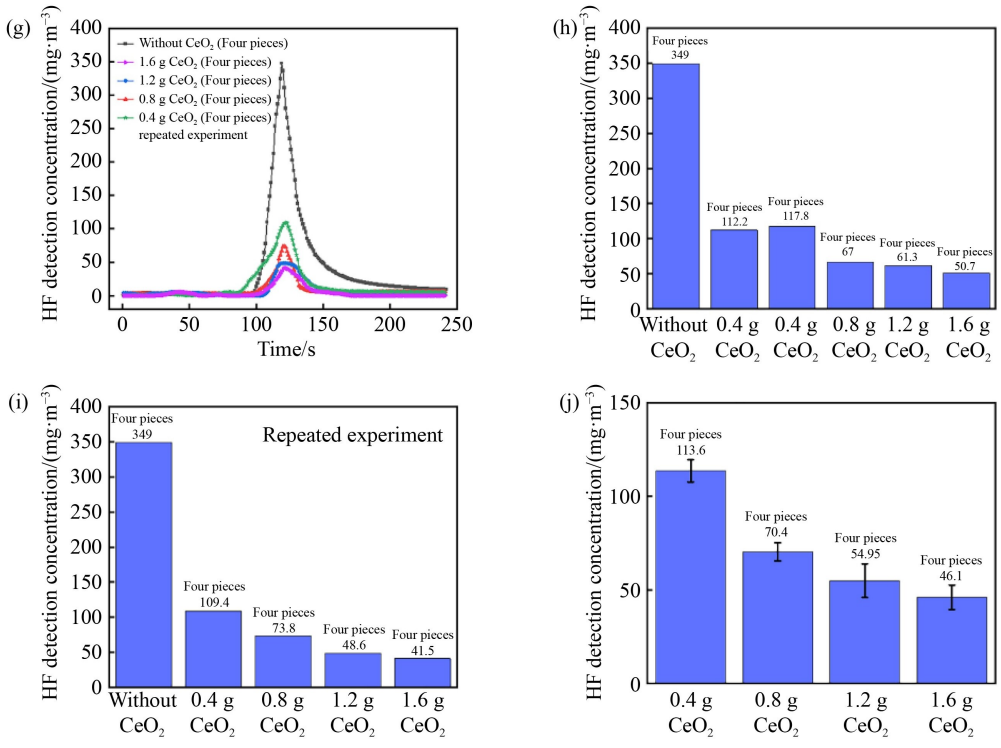

Fig. 4 HF gas detection concentration.

(a) Four pieces of filter without CeO_2 coated; (b) two pieces of filter coated with 0.4 g CeO_2; four pieces of filter coated with (c) 0.4 g; (d) 0.8 g; (e) 1.2 g; (f) 1.6 g CeO_2 and (g) repeated experiments; (h) comparison of the highest instantaneous HF concentrations; (i) comparison of the highest instantaneous HF concentrations (repeated experiments); (j) average of the highest instantaneous HF concentrations.

Table 1 Comparison of the highest instantaneous adsorption of HF gas during lithium-ion battery thermal runaway

Four pieces of filter	HF concentration /(mg·m^{-3})	Adsorption efficiency	HF concentration (repeat) /(mg·m^{-3})	Adsorption efficiency (repeat)
0.4 g CeO_2	117.8	66.25%	109.4	68.66%
0.8 g CeO_2	67	80.81%	73.8	78.86%
1.2 g CeO_2	61.3	82.24%	48.6	86.08%
1.6 g CeO_2	50.7	85.47%	41.5	88.11%

respectively. These results are basically consistent with the findings of the first experiment.

From the experiments, it can be seen that the rapid adsorption effect of the filters for HF gas improves as the mass of CeO_2 coating increases. However, the enhancement in the adsorption becomes less significant once the CeO_2 coating reaches a certain point. As shown in Table 1, the increase in instantaneous HF removal rate is relatively small when the CeO_2 mass increases from 1.2 to 1.6 g (82.24% to 85.47%). Based on these results, 1.2 g of CeO_2 appears to be an optimal choice in terms of cost-effectiveness.

In addition to adsorption properties, the reuse of adsorbents is also crucial. To advance the potential application of CeO_2 materials for the rapid adsorption of toxic gases from LIBs during thermal runaway, it is important that they function effectively in high temperature environments. The ability of CeO_2 to regenerate at high temperatures was briefly investigated, with the hope that it would be useful for future experiments. Therefore, 1.2 g of CeO_2 coated on four pieces of filters, after one adsorption cycle, was regenerated and reused. The adsorbed CeO_2 was heated at 800 °C in air for 60 min to remove the fluorine element.

Figures 5(a) and 5(b), along with Tables 2 and 3, show the SEM images and corresponding EDX data after one adsorption and regeneration cycle of the flowerlike CeO_2 microspheres. These images reveal that the CeO_2 particles still maintained their spherical structure. However, the pores seem to be partially blocked by some substances, which may include CMC binders or products produced by the adsorption of thermal runaway gas of lithium-ion battery and vaporized electrolyte. In addition, the EDX data (Tables 2 and 3, Figs. S2 and S3) show that the 60-min treatment at 800 °C effectively removed fluorine from the CeO_2 microspheres, thus achieving regeneration.

As shown in Fig. 6 and Table 4, the regenerated flowerlike CeO_2 microspheres still continue to demonstrate effective adsorption, with the highest HF detection concentration detected being 74.3 mg/m^3 and the highest instantaneous HF removal rate reaching 78.71%. This simple investigation confirms that, after HF adsorption, the fluorine element can be removed by

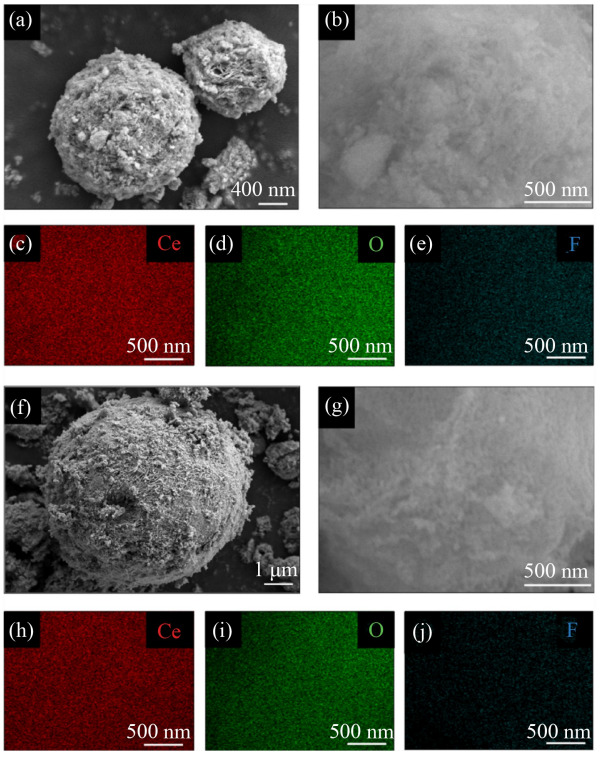

Fig. 5 SEM images and corresponding EDX mapping results. (a) SEM image of flowerlike CeO_2 microspheres after one adsorption cycle; (b–e) EDX mapping results; (f) SEM image of flowerlike CeO_2 microspheres after regeneration; (g–j) EDX mapping results.

heating, enabling the regeneration of adsorbent. Furthermore, the regenerated CeO_2 maintains strong adsorption performance.

Based on the results from the above experiments, additional adsorption and corresponding regeneration experiments were conducted to further evaluate the reuse ability of flowerlike CeO_2. In this experiment, 0.8 g of CeO_2 was uniformly distributed on two pieces of nickel foam to create two filters which were used to adsorb HF gas produced during thermal runaway of a single 5 Ah lithium iron phosphate ($LiFePO_4$) soft-pack battery over several cycles, in order to investigate the adsorption capacity of the filters. As shown in Fig. 7, the highest instantaneous HF gas concentrations observed during thermal runaway of the first to 10th 5 Ah $LiFePO_4$ soft-pack batteries were 65.5, 67.5, 75.9, 87.2, 109.8, 110.9, 125.1, 195.5, 208.6, and 220.2 mg/m^3, respectively. The corresponding highest instantaneous removal rates were 81.23%, 80.66%, 78.25%, 75.01%, 68.54%, 68.22%, 64.15%, 43.98%, 40.23%, and 36.91%, respectively.

Repeated experiments are shown in Fig. S9, where the highest instantaneous HF gas concentrations during thermal runaway of the first to 10th 5 Ah $LiFePO_4$ soft-pack batteries were 62.8, 69.7, 74.1, 89.1, 101.8, 110.5, 137.6, 221.7, 234.6, and 242.5 mg/m^3, respectively. The corresponding highest instantaneous removal rates were 82.01%, 80.03%, 78.77%, 74.47%, 70.83%, 68.22%, 60.57%, 36.48%, 32.78%, and 30.52%, respectively.

Following this, the 0.8 g of CeO_2, which had undergone multiple adsorption cycles, was placed in an air environment at 800 °C for 60–120 min for regeneration. Figure S10 shows the XPS data of the flowerlike CeO_2 after multiple adsorptions and regeneration. From Table S4, it can be seen that

Table 2 EDX data of CeO_2 microspheres after one adsorption cycle

Element	wt%	Atomic%
O K	18.3	63.89
Ce L	80.31	32.02
F K	1.39	4.09
Totals	100	

Table 3 EDX data of CeO_2 microspheres after regeneration

Element	wt%	Atomic%
O K	20.35	69.12
Ce L	79.65	30.88
F K	0	0
Totals	100	

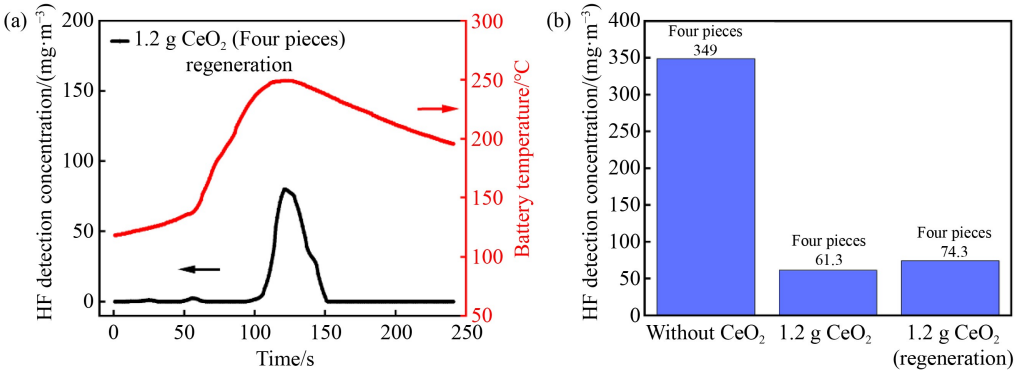

Fig. 6 Detection concentration of HF gas for four pieces of filters coated. (a) 1.2 g CeO_2 (regeneration); (b) comparison of the highest instantaneous HF concentrations.

maintaining flowerlike CeO_2 at 800 °C for 60–120 min in air can effectively remove the fluorine element. After 120 min, the fluorine content inside the flowerlike CeO_2 was reduced to 0.25%, which was selected for resorption experiments.

Table 4 Comparison of the highest instantaneous adsorption of HF gas from lithium-ion battery during thermal runaway before and after regeneration

1.2 g CeO_2 (Four pieces of filters)	HF concentration	Adsorption efficiency
Before regeneration	61.3 mg/m^3	82.24%
After regeneration	74.3 mg/m^3	78.71%

As shown in Figs. 8(a) and 8(b), after one adsorption cycle, the flowerlike structure of the CeO_2 microspheres is still visible, though there are noticeable agglomerates inside. However, as observed in Figs. 8(d) and 8(e), after ten adsorptions, the pores of the flowerlike CeO_2 microsphere seem to be completely blocked, and the structure looks more like a solid sphere. Upon regeneration (Fig. 5(f)), the flowerlike structure is retained after one adsorption, but after 10 adsorptions and regeneration (Figs. 8(g), (h), (j), and (k)), the flowerlike CeO_2 structure is transformed into smaller particles, which aggregate into spherical formations. This

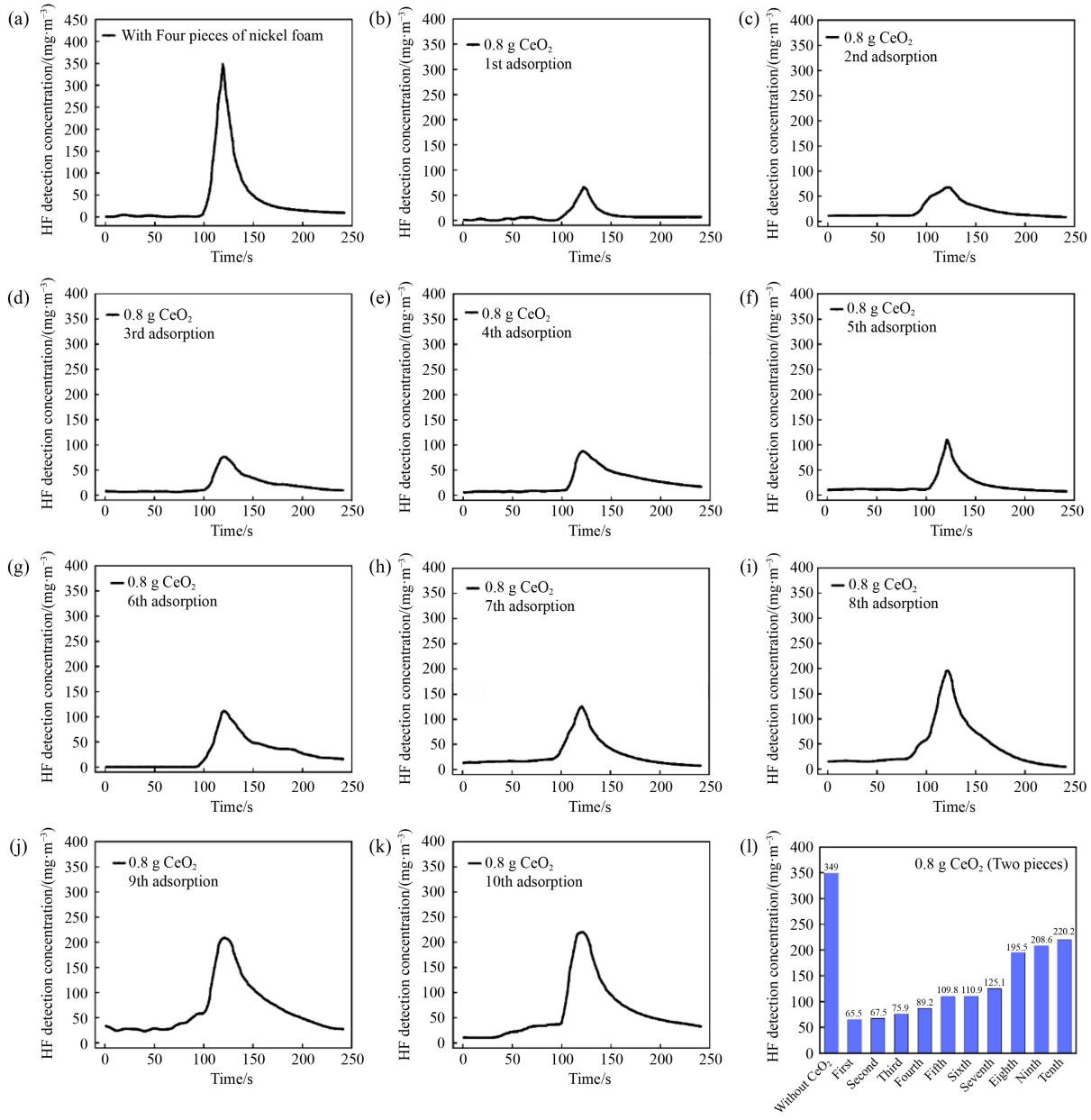

Fig. 7 HF gas detection concentrations.

(a) Without CeO_2; (b) after 1st adsorption; (c) after 2nd adsorption; (d) after 3rd adsorption; (e) after 4th adsorption; (f) after 5th adsorption; (g) after 6th adsorption; (h) after 7th adsorption; (i) after 8th adsorption; (j) after 9th adsorption; (k) after 10th adsorption; (l) comparison of the highest instantaneous HF concentrations.

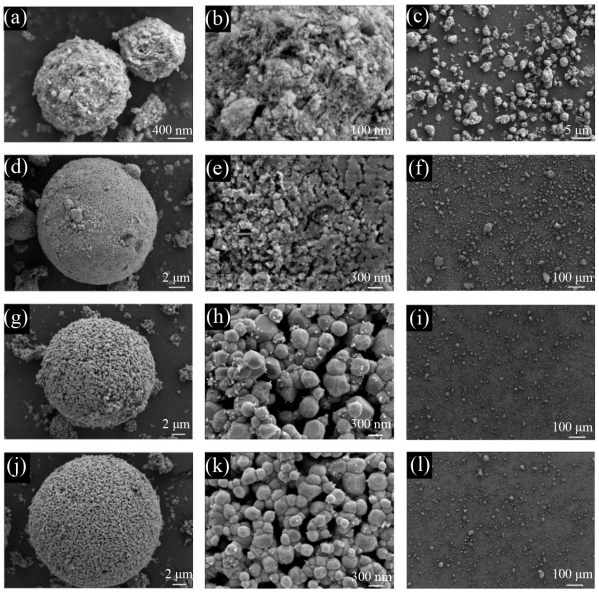

Fig. 8 SEM images of CeO_2 microspheres.
(a, b, c) after 1 adsorption; (d, e, f) after 10 adsorptions; (g, h, i) regeneration after 10 adsorptions (800 °C for 60 min); (j, k, l) regeneration after 10 adsorptions (800 °C for 120 min).

transformation is likely due to the removal of the fluorine element from the CeO_2 lattice. After 10 adsorptions, the elemental fluorine content inside the flowerlike CeO_2 is higher (9.55%), which may account for the significant morphological changes upon regeneration. The mechanism of this structural transformation remains unclear and requires further investigation.

The 0.8 g of CeO_2 coated on two pieces of filters, after 10 adsorption cycles, was regenerated at 800 °C for 120 min. The HF gas concentration detection during the adsorption experiment after CeO_2 regeneration is shown in Fig. 9. The highest instantaneous HF gas concentrations during the thermal runaway of the 1st to 3rd 5 Ah $LiFePO_4$ soft-pack batteries were 83.4, 127.6, and 130.7 mg/m^3, respectively. The corresponding highest instantaneous removal rates were 76.11%, 63.44%, and 62.55%. These results provide further in-depth evidence of the regeneration and reuse potential of flowerlike CeO_2 for HF gas adsorption.

3.3 Possible adsorption mechanism analysis

CeO_2 typically has catalytic activity for CO oxidation above 200 °C [39]. However, as shown in Fig. S6, the gas temperature during thermal runaway can reach a maximum of 88.9 °C, well below 200 °C. Therefore, CO oxidation catalysis by CeO_2 is not considered relevant in this context. Related experimental studies will be conducted in the future.

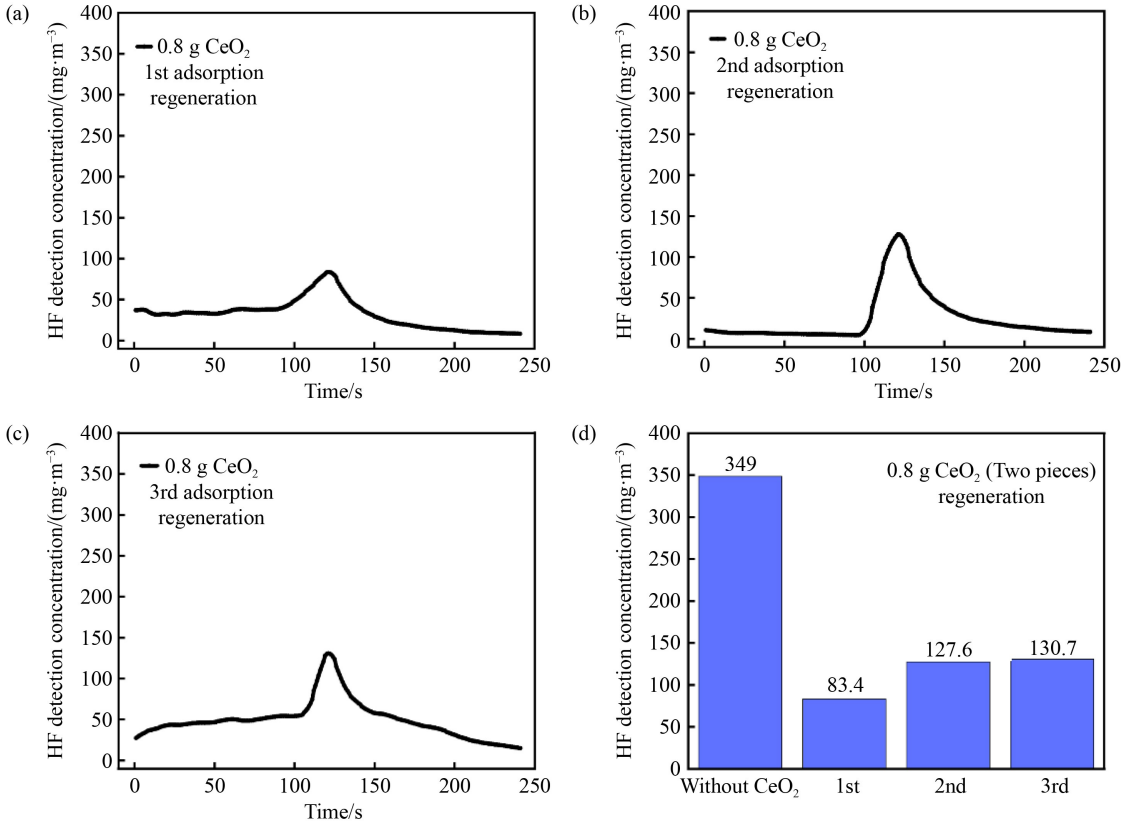

Fig. 9 HF gas detection concentrations (regeneration).
(a) After 1st adsorption; (b) after 2nd adsorption; (c) after 3rd adsorption; (d) comparison of the highest instantaneous HF concentrations.

The possible adsorption mechanism of flowerlike CeO_2 microspheres for HF gas in the high-temperature hazardous gas generated by LIBs during thermal runaway is briefly discussed. In the field of polluted water purification, both outer and inner sphere complexation are known to play an important role in fluoride removal by CeO_2 [40]. To further study the removal mechanism of flowerlike CeO_2 for HF gas, XPS was performed on CeO_2 samples before and after a single adsorption.

Figures 10(a) and 10(e) show the 3D spectra of Ce before and after a single adsorption, respectively. The peaks at 885, and 903.4 eV correspond to the Ce^{3+} oxidation state (blue line), while the peaks at 882.5, 889, 898.9, 901.4, 908, and 917.2 eV correspond to the Ce^{4+} oxidation state (red line). This observation suggests a certain oxygen deficiency in the flowerlike CeO_2 structure [41]. The ionic radii of F^- (0.133 nm) and O^{2-} (0.140 nm) are nearly identical in size [42], implying that F^- ions from HF gas could displace O^{2-} ions in the cerium matrix via an ion exchange process. This ion exchange may disrupt the charge equilibrium, promoting the reduction of Ce^{4+} to Ce^{3+}, which is confirmed by the increased proportion of Ce^{3+} in the flowerlike CeO_2 after adsorption (Table S5). Surface defects, particularly oxygen vacancies from the Ce^{3+}/Ce^{4+} transition, significantly impact charge transfer and surface chemisorption, thus enhancing fluoride adsorption [43].

HF gas adsorption increases the proportion of Ce^{3+} within the ceria structure, indicating the formation of additional oxygen vacancies. Thus, it is likely that oxygen vacancies promote easier Ce^{3+}-F complexation and ion exchange. When fewer oxygen vacancies are present, the ability of F^- to enter these oxygen vacancies and form complexes with Ce^{3+} is reduced, which may slow down the adsorption rate [45,46]. This phenomenon has also been reported previously [40,44].

The peaks at 529.4 eV in Figs. 10(b) and 10(f) correspond to the Ce-O band, mainly associated with surface lattice oxygen (Ce-O). It can be observed that the Ce-O ratio decreases after a single adsorption (Table S5), further supporting the idea that F^- replaces O^{2-} in CeO_2. Figure 10(h) shows the F1s XPS spectrum after adsorption by flowerlike CeO_2 microspheres, where the F 1s content increased from 0% to 3.36%. The fluorine peak at 684.1 eV, with binding energies between 684 and 685.5 eV, is characteristic of the metallic fluorine bond [45], which confirms the adsorption of fluorine on the flowerlike CeO_2 microspheres.

The flowerlike CeO_2 microspheres also have an open 3D porous structure with a large specific surface area and pore volume (129.8 m^2/g, 0.29 cm^3/g), which is conducive to gas transport.

Based on the following two premises: a low percentage of Ce^{3+} (e.g., below 20%) suggests that few oxygen vacancies are present, and the adsorbed substance is HF gas or other fluoride containing H^+ ions, it can be inferred from the X-ray photoelectron spectroscopy results that the adsorption of HF gas by flowerlike CeO_2 occurs in two steps. As shown in Fig. 11, first, HF gas molecules enter the channel of the 3D porous structure of flowerlike CeO_2, where they are physically adsorbed. This serves as the foundation for subsequent chemical adsorption. Second, as the F and H atoms in the HF molecules dissociate and migrate, some F^- ions enter the oxygen vacancies to complex with Ce^{3+}. Meanwhile, the majority of F^- replace O^{2-} and bind to the cerium oxide lattice, releasing two electrons in the process. These free electrons initiate the reduction of Ce^{4+} to Ce^{3+}, which then associates with F^-. The H atoms from HF molecules bond to O atoms, leading to the production and release of H_2O molecules.

3.4 Discussion of potential adsorbent materials

Currently, few studies have focused on the rapid adsorption of toxic gases produced by LIBs during thermal runaway. When selecting adsorbent materials for such applications, three key factors should be considered:

(1) Temperature resistance: The adsorbent material must withstand high temperatures without desorbing. For example, carbon materials, though widely used for gas adsorption, can easily react in high-temperature environments, while NaF, commonly used for HF gas adsorption, desorbs above 250 °C.

(2) Economic considerations: The economic viability of the adsorbent material is crucial. This includes not only the cost of the material itself but also its regeneration performance and effectiveness. Alumina, for instance, is currently a promising material for HF gas adsorption due to its affordability and efficiency.

(3) Adsorption potential for major toxic gases: The material must exhibit strong adsorption capabilities for the toxic gases, such as CO and HF from LIBs during thermal runaway. CeO_2 is a promising candidate due to its ability to form oxygen vacancies, which enable it to oxidize CO to CO_2 above 200 °C [39]. The temperature required for this reaction can be further lowered when Pt-loaded catalysts are used on Cu-modified CeO_2 supports (below 100 °C) [47].

Given these considerations, future research on materials for the adsorption of toxic gases from LIBs during thermal runaway may focus on two areas points:

(1) Material selection: Materials like CeO_2, Al_2O_3, and molecular sieves should be further explored. These materials either have a well-established research base with wide industrial applications or exhibit unique potential for use in LIBs gas adsorption during thermal runaway. The complex nature of the gases emitted during thermal runaway necessitates an in-depth investigation into the adsorption capabilities of these materials, with an emphasis on their capacity to adsorb a variety of toxic gases.

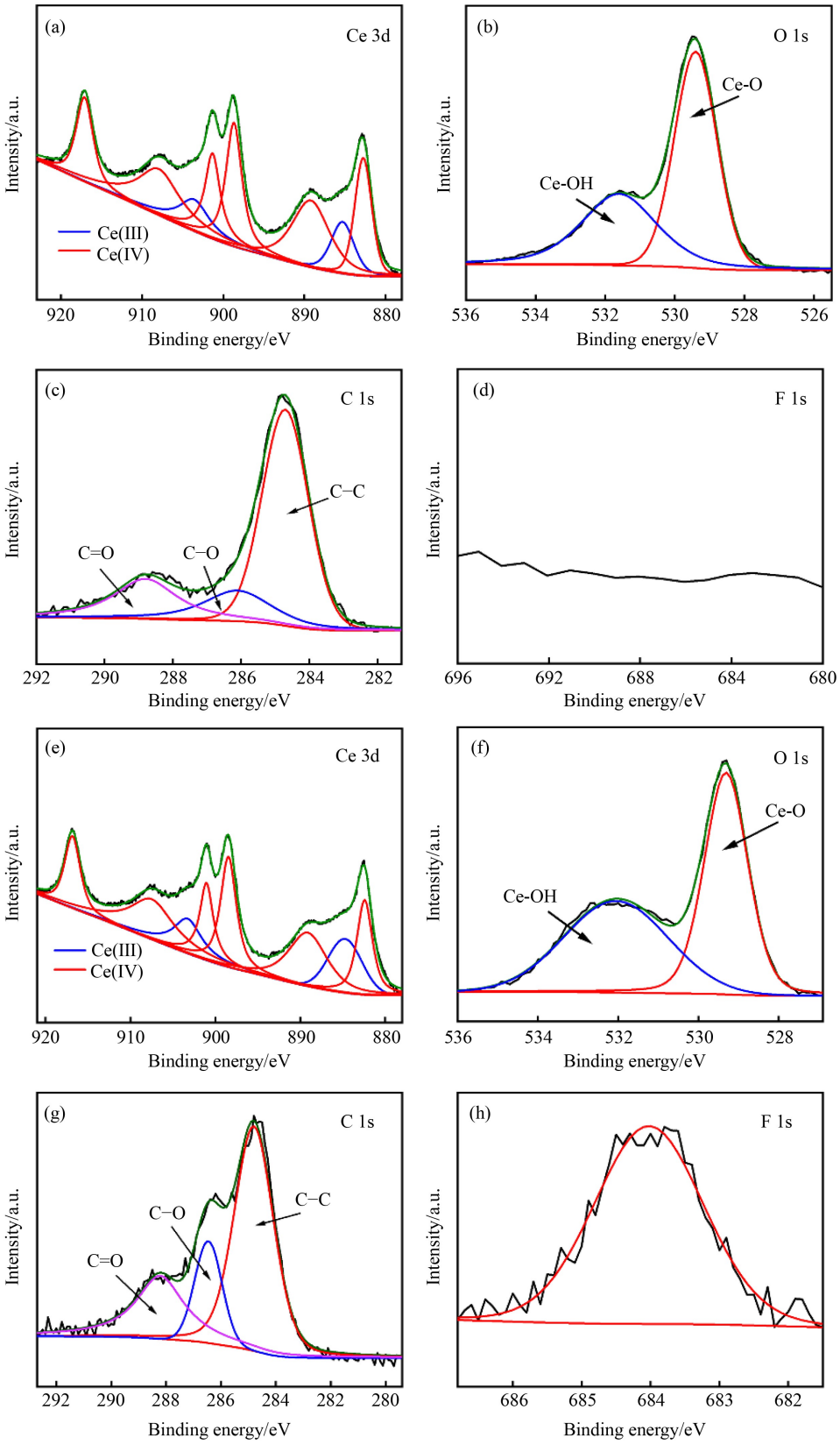

Fig. 10 XPS spectra of the flowerlike CeO_2 microspheres.
Before adsorption: (a) Ce 3d; (b) O 1s; (c) C 1s; (d) F 1s; after one adsorption: (e) Ce 3d; (f) O 1s; (g) C 1s; (h) F 1s.

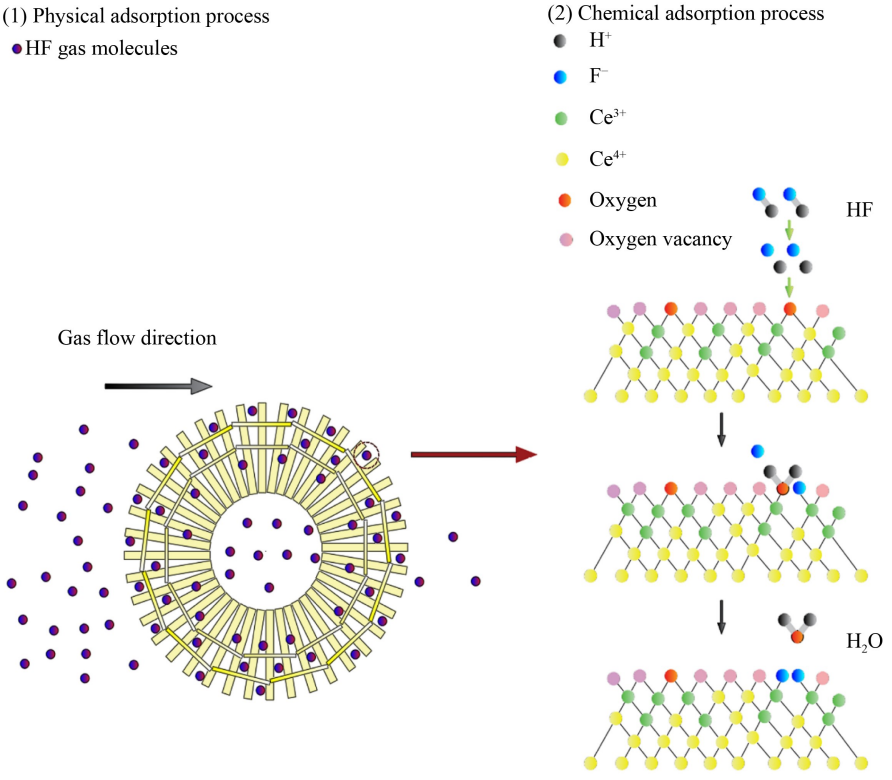

Fig. 11 Possible mechanisms of HF adsorption in CeO_2 microsphere.

(2) Material structure and modification: The structure and modification of the materials are crucial for enhancing their adsorption performance. Improving the specific surface area through optimal structural design can increase the contact area between the material and the gas, enhancing its adsorption capacity. For instance, ball milling techniques can effectively reduce particle size, increasing the surface area and porosity, thereby improving adsorption. However, smaller particle sizes may lead to agglomeration, which reduced the material's activity and adsorption capacity [48]. For certain materials, such as flowerlike CeO_2, further ball milling may not be effective, as it could damage the structure and reduce the material's specific surface area and porosity. Furthermore, loading materials like Cu, Mg, or Pt can enhance the material's activity, further boosting its adsorption capacity.

4 Conclusions

This study investigates the rapid adsorption of HF gas generated during the thermal runaway of LIBs and the regeneration of the adsorbed CeO_2 microspheres. First, a simple test device and method were designed to evaluate the gas adsorption performance of LIBs during thermal runaway. Then, flowerlike CeO_2 microspheres were synthesized via a hydrothermal method. These microspheres possess an open 3D porous structure with a large specific surface area and pore volume (129.8 m^2/g, 0.29 cm^3/g^1), demonstrating significant adsorption capability for toxic HF gas produced during thermal runaway of LIBs.

For a 5 Ah $LiFePO_4$-based lithium-ion battery undergoing thermal runaway, the highest instantaneous removal rate of HF gas reached 82.24% using four pieces of nickel foam filter coated with 1.2 g of CeO_2. The adsorption process is driven by the ion exchange mechanism, where F^- ions in the HF gas replace O^{2-} ions in the cerium lattice. In addition, the regeneration and reuse capabilities of flowerlike CeO_2 microspheres were studied. The fluorine element can be effectively removed by maintaining CeO_2 filters at 800 °C for 60–120 min. After a single adsorption and subsequent regeneration, the highest instantaneous removal rate of HF was approximately 78.71% for the 1.2 g of CeO_2, and after 10 adsorption and regeneration cycles, the 0.8 g of CeO_2 maintained a removal rate of 76.11%.

This study provides valuable insights into the prevention of toxic gas diffusion during lithium battery fires, offering a potential solution for protecting firefighters' respiratory health.

Acknowledgements This work was supported by the National Key R&D Program of China (Grant No. 2023YFE0115800), and the National Natural Science Foundation of China (Grant No. 52472271), the National Key Research and Development Program of China (Grant No.

2023YFC3009504), the Basic Research Project of China Academy of Civil Aviation Science and Technology (Grant No. x242060302244), and the Key Program of the Joint Fund for Civil Aviation Research with National Natural Science Foundation of China (Grant No. U2033204).

Competing Interests The authors declare that they have no competing interest.

Electronic Supplementary Material Supplementary material is available in the online version of this article at https://doi.org/10.1007/s11708-025-1014-4 and is accessible for authorized users.

References

1. Grey C P, Hall D S. Prospects for lithium-ion batteries and beyond—A 2030 vision. Nature Communications, 2020, 11(1): 6279
2. Zhang X, Feng J, Cai F, et al. A novel state of health estimation model for lithium-ion batteries incorporating signal processing and optimized machine learning methods. Frontiers in Energy, 2024, early access, doi:10.1007/s11708-024-0969-x
3. Ding L, Chen Y, Sheng Y, et al. Eliminating hydrogen fluoride through piperidine-doped separators for stable Li metal batteries with nickel-rich cathodes. Angewandte Chemie International Edition, 2024, 63(51): e202411933
4. Wang H, Xu H, Zhang Z, et al. Fire and explosion characteristics of vent gas from lithium-ion batteries after thermal runaway: A comparative study. eTransportation, 2022, 13: 100190
5. Zhou W, Li G, Zhao H, et al. Experimental study of explosion parameters of hybrid mixture caused by thermal runaway of lithium-ion battery. Process Safety and Environmental Protection, 2023, 178: 872–880
6. Wei G, Huang R, Zhang G, et al. A comprehensive insight into the thermal runaway issues in the view of lithium-ion battery intrinsic safety performance and venting gas explosion hazards. Applied Energy, 2023, 349: 121651
7. Zhao L, Hou J, Feng X, et al. The trade-off characteristic between battery thermal runaway and combustion. Energy Storage Materials, 2024, 69: 103380
8. Feng X, Ren D, He X, et al. Mitigating thermal runaway of lithium-ion batteries. Joule, 2020, 4(4): 743–770
9. Wang Q, Mao B, Stoliarov S I, et al. A review of lithium ion battery failure mechanisms and fire prevention strategies. Progress in Energy and Combustion Science, 2019, 73: 95–131
10. Larsson F, Bertilsson S, Furlani M, et al. Gas explosions and thermal runaways during external heating abuse of commercia lithium-ion graphite-$LiCoO_2$ cells at different levels of ageing. Journal of Power Sources, 2018, 373: 220−231
11. Bugryniec P J, Resendiz E G, Nwophoke S M, et al. Review of gas emissions from lithium-ion battery thermal runaway failure—Considering toxic and flammable compounds. Journal of Energy Storage, 2024, 87: 111288
12. Claassen M, Bingham B, Chow J C, et al. Characterization of lithium-ion battery fire emissions—Part 1: Chemical composition of fine particles ($PM_{2.5}$). Batteries, 2024, 10(9): 301
13. Claassen M, Bingham B, Chow J C, et al. Characterization of lithium-ion battery fire emissions—Part 2: Particle size distributions and emission factors. Batteries, 2024, 10(10): 366
14. Yuan L, Dubaniewicz T, Zlochower I, et al. Experimental study on thermal runaway and vented gases of lithium-ion cells. Process Safety and Environmental Protection, 2020, 144: 186–192
15. Qin P, Jia Z, Wu J, et al. The thermal runaway analysis on $LiFePO_4$ electrical energy storage packs with different venting areas and void volumes. Applied Energy, 2022, 313: 118767
16. Larsson F, Andersson P, Blomqvist P, et al. Toxic fluoride gas emissions from lithium-ion battery fires. Scientific Reports, 2017, 7(1): 10018
17. Zhang L, Duan Q, Meng X, et al. Experimental investigation on intermittent spray cooling and toxic hazards of lithium-ion battery thermal runaway. Energy Conversion and Management, 2022, 252: 115091
18. Krebs R, Owens J, Luckarift H. Formation and detection of hydrogen fluoride gas during fire fighting scenarios. Fire Safety Journal, 2022, 127: 103489
19. Yang H, Zhuang G V, Ross P N Jr. Thermal stability of $LiPF_6$ salt and Li-ion battery electrolytes containing $LiPF_6$. Journal of Power Sources, 2006, 161(1): 573–579
20. Kawamura T, Okada S, Yamaki J. Decomposition reaction of $LiPF_6$-based electrolytes for lithium ion cells. Journal of Power Sources, 2006, 156(2): 547–554
21. Larsson F, Andersson P, Blomqvist P, et al. Characteristics of lithium-ion batteries during fire tests. Journal of Power Sources, 2014, 271: 414–420
22. Larsson F, Anderson J, Andersson P, et al. Thermal modelling of cell-to-cell fire propagation and cascading thermal runaway failure effects for lithium-ion battery cells and modules using fire walls. Journal of the Electrochemical Society, 2016, 163(14): A2854–A2865
23. Kahya N, Erim F B. Removal of fluoride ions from water by cerium-carboxymethyl cellulose beads doped with CeO_2 nanoparticles. International Journal of Biological Macromolecules, 2023, 242: 124595
24. Kang D, Yu X, Ge M. Morphology-dependent properties and adsorption performance of CeO_2 for fluoride removal. Chemical Engineering Journal, 2017, 330: 36–43
25. Wang Y, Luo X. Efficient adsorptive removal of low concentration fluoride ions from water by cellulose beads with trapped CeO_2 nanoparticles. Journal of Environmental Chemical Engineering, 2024, 12(5): 113180
26. Singh S K, Pahi S, Behera A, et al. Studies of hybrid ceria polypyrrole CPP-2 composite for effective defluoridation from potable water. Colloids and Surfaces. A, Physicochemical and Engineering Aspects, 2024, 702: 135026
27. Liu X, Rehman D, Shu Y, et al. Selective fluoride removal from groundwater using CNT-CeO_2 electrodes in capacitive deionization (CDI). Chemical Engineering Journal, 2024, 482: 149097
28. Wang T, Gang H, Cao Y, et al. Hydrous CeO_2 polypyrrole nanocomposite as a stable and efficient adsorbent for defluoridation of acidic wastewater. Journal of Materials Science, 2023, 58(19): 7895–7914
29. Jian S, Shi F, Hu R, et al. Electrospun magnetic La_2O_3–CeO_2–Fe_3O_4 composite nanofibers for removal of fluoride

from aqueous solution. Composites Communications, 2022, 33: 101194

30. Chen F, Lv F, Li H, et al. Evaluation of fluoride adsorption in solution by synthetic Al_2O_3/CeO_2: A fixed-bed column study. Water Environment Research, 2021, 93(11): 2559–2575
31. Wang K, Lei H, Muhammad Y, et al. Controlled preparation of cerium oxide loaded slag-based geopolymer microspheres (CeO_2@ SGMs) for the adsorptive removal and solidification of F^- from acidic waste-water. Journal of Hazardous Materials, 2020, 400: 123199
32. Wang F, Wang K, Muhammad Y, et al. Preparation of CeO_2@ SiO_2 microspheres by a non-sintering strategy for highly selective and continuous adsorption of fluoride ions from wastewater. ACS Sustainable Chemistry & Engineering, 2019, 7(17): 14716–14726
33. Wilklow-Marnell M, Jones W D. Catalytic oxidation of carbon monoxide by α-alumina supported 3 nm cerium dioxide nanoparticles. Molecular Catalysis, 2017, 439: 9–14
34. Cha X, He J, Fu Y, et al. Carbonate-mediated Mars-van Krevelen mechanism on Cu_xO/CeO_2 catalysts for boosting CO oxidation. Chemical Engineering Journal, 2024, 501: 157643
35. Sun C, Sun J, Xiao G, et al. Mesoscale organization of nearly monodisperse flowerlike ceria microspheres. Journal of Physical Chemistry B, 2006, 110(27): 13445–13452
36. Liao Z, Zhang S, Li K, et al. Hazard analysis of thermally abused lithium-ion batteries at different state of charges. Journal of Energy Storage, 2020, 27: 101065
37. Andersson P, Blomqvist P, Lorén A, et al. Using Fourier transform infrared spectroscopy to determine toxic gases in fires with lithium-ion batteries. Fire and Materials, 2016, 40(8): 999–1015
38. Sun J, Li J, Zhou T, et al. Toxicity, a serious concern of thermal runaway from commercial Li-ion battery. Nano Energy, 2016, 27: 313–319
39. Vincent J L, Crozier P A. Atomic level fluxional behavior and activity of CeO_2-supported Pt catalysts for CO oxidation. Nature Communications, 2021, 12(1): 5789
40. Rashid U S, Das T K, Sakthivel T S, et al. GO-CeO_2 nanohybrid for ultra-rapid fluoride removal from drinking water. Science of the Total Environment, 2021, 793: 148547
41. Seal S, Jeyaranjan A, Neal C J, et al. Engineered defects in cerium oxides: tuning chemical reactivity for biomedical, environmental, & energy applications. Nanoscale, 2020, 12(13): 6879–6899
42. Slater J C. Atomic radii in crystals. Journal of Chemical Physics, 1964, 41(10): 3199–3204
43. Vento-Lujano E, González L A. Defect-induced modification of band structure by the insertion of Ce^{3+} and Ce^{4+} in $SrTiO_3$: A high-performance sunlight-driven photocatalyst. Applied Surface Science, 2021, 569: 151044
44. Ahmad S, Gopalaiah K, Chandrudu S N, et al. Anion (fluoride)-doped ceria nanocrystals: Synthesis, characterization, and its catalytic application to oxidative coupling of benzylamines. Inorganic Chemistry, 2014, 53(4): 2030–2039
45. Nair S, Bose R, Durani S, et al. An eco-friendly and low-cost methodology for fluoride adsorption using synthesized and characterized ceria-impregnated activated graphite (CIAG). Chemicke Zvesti, 2024, 78(6): 3883–3906
46. Pan Y, Liu X, Zhang M, et al. The impact of redox annealing on intrinsic properties and fluoride adsorption performance of CeO_2 nanomaterials. Chemical Engineering Journal, 2023, 476: 146347
47. Liu X, Jia S, Yang M, et al. Activation of subnanometric Pt on Cu-modified CeO_2 via redox-coupled atomic layer deposition for CO oxidation. Nature Communications, 2020, 11(1): 4240
48. Hamaloğlu K Ö, Tosun R B, Ulu S, et al. Monodisperse-porous cerium oxide microspheres as a new support with appreciable catalytic activity for a composite catalyst in benzyl alcohol oxidation. New Journal of Chemistry, 2021, 45(4): 2019–2029